Bioactive Materials 40 (2024) 168–181

Contents lists available at ScienceDirect

Bioactive Materials

journal homepage: www.keaipublishing.com/en/journals/bioactive-materials

Multiscale engineered artificial compact bone *via* bidirectional freeze-driven lamellated organization of mineralized collagen microfibrils

Lingwenyao Kong [a,1], Yonggang Zhao [b,1], Yang Xiong [c], Junlin Chen [a], Shuo Wang [a], Ziming Yan [d], Huibin Shi [d], Zhanli Liu [d], Xiumei Wang [a,*]

[a] State Key Laboratory of New Ceramics and Fine Processing, Key Laboratory of Advanced Materials of Ministry of Education, School of Materials Science and Engineering, Tsinghua University, Beijing, 100084, China
[b] State Key Laboratory for Performance and Structure Safety of Petroleum Tubular Goods and Equipment Materials, Tubular Goods Research Institute of CNPC, Xi'an, 710077, China
[c] Department of Orthopedics, Dongzhimen Hospital, Beijing University of Chinese Medicine, Beijing, China
[d] School of Aerospace Engineering, Tsinghua University, Beijing, 100084, China

ARTICLE INFO

Keywords:
Artificial compact bone
Bidirectional freeze-casting
Mineralized collagen microfibril
Hierarchical structures

ABSTRACT

Bone, renowned for its elegant hierarchical structure and unique mechanical properties, serves as a constant source of inspiration for the development of synthetic materials. However, achieving accurate replication of bone features in artificial materials with remarkable structural and mechanical similarity remains a significant challenge. In this study, we employed a cascade of continuous fabrication processes, including biomimetic mineralization of collagen, bidirectional freeze-casting, and pressure-driven fusion, to successfully fabricate a macroscopic bulk material known as artificial compact bone (ACB). The ACB material closely replicates the composition, hierarchical structures, and mechanical properties of natural bone. It demonstrates a lamellated alignment of mineralized collagen (MC) microfibrils, similar to those found in natural bone. Moreover, the ACB exhibits a similar high mineral content (70.9 %) and density (2.2 g/cm^3) as natural cortical bone, leading to exceptional mechanical properties such as high stiffness, hardness, and flexural strength that are comparable to those of natural bone. Importantly, the ACB also demonstrates excellent mechanical properties in wet, outstanding biocompatibility, and osteogenic properties *in vivo*, rendering it suitable for a broad spectrum of biomedical applications, including orthopedic, stomatological, and craniofacial surgeries.

1. Introduction

Natural mineralized biomaterials, such as bone, enamel, and nacre, are typically composed of simple ingredients, but demonstrate remarkable mechanical performances that far exceed those of their individual components and their mixture [1–5]. This is primarily attributed to the effective integration of soft and hard phases and their multiscale organization, ranging from the nano-to macro level, resulting in a sophisticated and compact architecture [6–8]. Therefore, the development of high-performance composite materials through biomimetic designs, inspired by the complex hierarchical organization of natural mineralized tissues, has garnered significant interest and attention [9–11].

Bone is the most prevalent and essential organic/inorganic hybrid nanomaterial in the human body [12]. It comprises 65 wt % inorganic components, 25 wt % organic components, and 10 wt % water [1]. Bone possesses a complex multilevel structure, consisting of collagen molecules and nano-hydroxyapatite (nHAp), which self-assemble from the bottom up into microfibrils, fibrils, fibers, fiber bundles, lamellae, osteons, and compact bone [13]. Collagen molecules self-assemble in parallel into microfibrils to modulate nHAp nucleation and growth on the specific sites at the molecular level and then span to higher hierarchies [14]. The molecular combination of collagen and nHAp, as well as the hierarchical organization of elaborated architectures at multiple length scales, contribute to the exceptional mechanical properties of bone, characterized by unique strength and toughness [15–18]. These properties have served as inspiration for the development of biomimetic

Peer review under responsibility of KeAi Communications Co., Ltd.
* Corresponding author.
E-mail address: wxm@mail.tsinghua.edu.cn (X. Wang).
[1] These authors contribute to the work equally.

https://doi.org/10.1016/j.bioactmat.2024.02.005
Received 2 November 2023; Received in revised form 12 January 2024; Accepted 6 February 2024

artificial bone grafts. However, the preparation of artificial compact bone materials that possess similar compositions, structures, and properties to natural cortical bone presents significant challenges yet holds great significance in biomedical applications [19–21].

In recent years, the development of high-strength bone materials has gained significant attention due to their potential to address clinical challenges associated with load-bearing applications in orthopedic and dental surgeries. A biomimetic and biodegradable synthetic bone material that highly resembles natural compact bone could effectively meet the demand, showing significant clinical implications. However, relevant studies on the development of high-strength bone materials composed of biomineralized collagen, excluding synthetic polymers, metals, and non-degradable ceramics have been sparsely reported. In our previous research [22], we proposed a "multiscale cascade regulation" strategy, which integrates multiple techniques including molecular self-assembly, electrospinning, and pressure-driven fusion to modulate the combination of collagen and nHAp from nano-to macrolevels to achieve the construction of a bulk artificial lamellar bone (ALB). The mineralized collagen-based ALB highly resembled the rotated plywood-like structure of natural lamellae, resulting in a favorable combination of lightweight, high strength, and toughness. However, the electrospinning technique imposes a limitation on both the maximum mineral content of ALB that is approximately 40% and the cross-linking process [23–25]. Consequently, the ALB is prone to rapid swelling and degradation *in vivo*, which limits its clinical applications. Therefore, one of the primary objectives of this study is to develop an artificial compact bone material with excellent mechanical properties and a slow degradation rate, capable of providing long-lasting mechanical support throughout the entire bone regeneration process. We expect to identify a facile method that can increase the nHAp content of the artificial compact bone material while preserving the lamellar structure, thus achieving a comparable density and improved mechanical properties and stability, tailored to meet the specific demands of various bone defect sites.

The bidirectional freezing technique, developed by Ritchie group [26–28], has been effectively utilized to construct intricate architectures like nacre and enamel, by which the assembly of small building blocks was driven into a porous lamellar structure. In this study, we combined the bidirectional freezing technique with molecular self-assembly of mineralized collagen and pressure-driven fusion for the first time to produce a macroscopic bulk artificial compact bone (ACB) material. The ACB material exhibits a lamellated alignment of mineralized collagen (MC) microfibrils. it replicates both the aligned MC fibrils and the lamellar structure found in natural bone, resulting in improved mechanical properties. Simultaneously, the high content of mineralized collagen microfibrils in the slurry used for bidirectional freezing ensures that the ACB material possesses a mineral content consistent with that of natural bone. Furthermore, the ACB material can be readily combined with other biocompatible polymers, ceramics, or bioactive molecules to produce a range of compact structural and functional biomaterials. These materials can be manufactured on a large scale for clinical translations. In general, the exceptional mechanical performance, biocompatibility, and bioactivities of the ACB material make it suitable for various biomedical applications, including orthopedic, stomatological, and craniofacial surgeries.

2. Materials and methods

2.1. Reagents

Type I collagen (Mw = 280 kDa) was purchased from Hebei Collagen Biotechnology Co., Ltd. (Atelocollagen from bovine skin), and used as received. The chemicals used in this study, including anhydrous calcium chloride ($CaCl_2$), sodium hydroxide (NaOH), orthophosphoric acid (H_3PO_4), calcium hydroxide ($Ca(OH)_2$), Tris-HCl ($C_4H_{11}NO_3$·HCl), ammonium hydroxide (NH_4OH), 1,1,1,3,3,3-Hexafluoro-2-propanol (HFIP), Poly (vinyl alcohol) (PVA, 87.0–89.0%, Mw = 3 kDa), glutaraldehyde, were all purchased from Sigma-Aldrich, Inc. (St. Louis, MO, USA). PDMS (Sylgard 184, Dow Corning, 184 Silicone Elastomer kit, Germany) wedges were obtained by mixing the polymer with the curing agent at a ratio of 10:1, then curing at room temperature for more than 12 h.

2.2. Preparation of MC microfibrils

The mineralized collagen microfibrils were synthesized according to the method reported previously [22]. Briefly, collagen was dissolved in 12 mM H_3PO_4 solution at a concentration of 0.03% (w/v) and stirred for more than 10 h to ensure complete dissolution. Separately, $Ca(OH)_2$ was completely dissolved in pre-cooled de-ionized water (20 mM) at 4 °C and stirred for 1 h. Then the collagen/H_3PO_4 and $Ca(OH)_2$ solutions were dropped slowly at a volume ratio of 1:1 (Ca/P = 1.67) into 10 M Tris-HCl buffer solution with pH 8.5 at 37 °C under gentle stirring for 24 h. The precipitate was centrifuged and washed with distilled water three times at 3000 rpm/min and then finally collected by centrifugation (Cence H2500R) at 16,000 rpm/min for 10 min.

2.3. Artificial compact bone fabrication

The first step is to prepare the slurry. Here, polyvinyl alcohol (0.9 g) was fully dissolved in deionized water (30 mL) in an oil bath at 95 °C and stirred for 3 h. Then, the slurry was obtained by mixing MC microfibril precipitate (wet, ~8 g) with PVA aqueous solution and stirring vigorously for 36 h.

The Teflon models (20 × 20 × 40 mm) with a PDMS wedge (20°) at the bottom were placed on a copper cold finger connected to a liquid nitrogen reservoir. Before freeze-casting, 0.1 mM glutaraldehyde was added to the slurry, stirred well, and then poured into the mold immediately, bidirectional freezing process promoted the lamellar ice crystals to grow preferentially under dual temperature gradients. A vertical gradient away from the cooling stage and a horizontal gradient from the thinner end to the thicker end of the PDMS wedge were formed, and the MC microfibril in the slurry was ejected from the generating solidification front and arranged in parallel each other along the ice layers. Finally, a long-range of porous aligned lamellar structure was generated after freeze-drying for 48 h, which was then compressed at 80 °C, 1500 MPa for 10 min to obtain the ACB. For comparison, we prepared a similar compact bone material with a randomly aligned structure (RCB) using a unidirectional freeze-casting process. A single vertical temperature gradient away from the cold finger was used, which promoted the preferential growth of ice crystals from bottom to top. Since the PDMS wedge did not create a horizontal temperature gradient, random nucleation of ice crystals took place on the entire cold surface of the finger, leading to the formation of multiple sub-millimeter structural domains in the final structure, each corresponding to a different orientation of lamellar ice crystals [26].

2.4. Morphological characterizations

The morphologies of the MC microfibrils, crack path and the fractured surfaces of the ACB were observed by SEM (Merlin Compact, Zeiss, Germany). All the samples were directly sputter-coated with a 10 nm Pt layer for SEM examinations. The suspension of MC microfibrils was isolated and washed with distilled water, and then dropped on copper grids after resuspension for TEM observation. For TEM investigations of the ACB bulk, FIB thin cuts along the longitudinal and cross-sections were prepared by using both a Vion™ Plasma FIB (Xe^+) and a Helios DualBeam at 2–30 keV (FEI, Eindhoven, Netherlands). The samples described above were observed by TEM (JEOL, Japan) at 200 kV. High-resolution TEM data were analyzed by using the Digital Micrograph software (Gatan company, USA).

The cell adhesion state on scaffolds was also examined by SEM. The

samples were fixed with 2.5% glutaraldehyde in PBS, followed by gradient dehydration from 30 % to 100% ethanol and critical point drying (Samdri-PVT-3D, America), and then sputter-coated with a 10 nm Pt layer for observation.

2.5. X-ray diffraction (XRD)

The inorganic minerals in the ACB bulks (prepared under different pressures of 20 MPa, 200 MPa, and 1500 MPa, denoted as *P*20, *P*200, *P*1500, respectively), collagen fibril, MC microfibril, and natural cortical bone were evaluated by an X-ray diffractometer (XRD) (D8 Discover, Bruker, Germany) with the condition of Cu $K\alpha 1$ radiation ($\lambda = 0.154056$ nm), 40 kV, and 200 mA. The range of diffraction angle 2θ was from 20° to 60° at a step scanning rate of 2°/min.

2.6. Thermogravimetric (TGA)

The mineral contents of different samples including the ACB bulks (prepared under different pressures of 1 MPa, 200 MPa, and 1500 MPa, denoted as *P*1, *P*200, *P*1500, respectively) and the MC microfibrils powder were evaluated using a thermogravimetric analyzer (Q5000IR, TA INSTRUMENTS, China). The samples (several dozen milligrams) were placed in a platinum open pan and weighed during the heating process at a rate of 10 °C/min from room temperature to 800 °C in air. Plot a curve of the change in quality versus temperature.

2.7. Fourier transform infrared spectroscopy (FTIR)

FTIR measurements of ALB bulks by different pressures were carried out using a spectrometer (Bruker, Germany). Frequency information of molecular vibrations is obtained by detecting the absorption intensity of ACB at different wave numbers (cm^{-1}), and this information can be used to identify and analyze the chemical composition and structure of materials, such as phosphate, amide I, and so on. The range of wavelength was 4000-600 cm^{-1}.

2.8. Raman spectroscopy

Raman spectroscopy measurements were carried out using a LabRAM HR Evolution (Horiba JobinYvon) with an incident laser with a 514 nm wavelength. A monochromatic laser beam is used as the excitation source, adjusting the optical system to focus the laser beam on the sample surface.

2.9. X-ray photon spectroscopy (XPS)

All the samples (ACB and MC microfibrils) were measured by an ESCALAB 250Xi (Thermo Figsher) device using a monochromatic Al KR X-ray source. The test procedure is performed in a high vacuum environment. Typically, the vacuum level is maintained below 10^{-7} mbars to minimize the interference of gas molecules on the experimental results.

2.10. Nanoindentation

The nano-hardness (*H*) and Young's modulus (E_y) of the ACB bulks in different directions were tested by a nanoindenter (Keysight G200, Keysight Technologies, China). The indenter force and displacement during the loading and unloading procedures were recorded with resolutions of 50 nN and 0.01 nm, respectively. The *H* and E_y under the static load were measured following the methods of Oliver-Pharr. The maximum load was maintained at 450 mN. Five positions were randomly selected and measured for each sample for average.

2.11. Micro-CT imaging

The ACB bulks were scanned by Micro-CT (InspexiosMX-90CT Plus, Shimadzu, Japan) at 90 kV accelerating voltage and the scanning step of 4 μm/pitch. During the scanning process, the X-ray source is fixed and the specimen is rotated 360° in a relatively stationary state for scanning and recording. The scanning speed is 10°/min. Additionally, the rat humeri with distal defects were scanned with a working distance of 80 mm and a scanning step of 10 μm/pitch. The scanning speed was increased to 20°/min to avoid tissue damage caused by prolonged service illumination. All data were analyzed using 3D reconstruction imaging *via* VGSTUDIO MAX 3.4 software with the same threshold.

2.12. Three-point bending test

Three-point bending tests were performed on an Instron (SFL, Shimadzu, Japan) testing machine. The ACB bulks (2 mm × 4 mm × 28 mm) were tested for the bending mechanical properties in in-plane and antiplane directions.

For single-edge notched beam (SENB) tests, the beam specimens with dimensions of about 2 mm × 4 mm × 28 mm were notched (about 2 mm length) on one edge side of the specimens. To investigate the fracture toughness of ACB, we have used a single-notched three-point bend test, which consists of a rectangular bar containing rounded notches (root radius ~200 μm) subjected to three-point bending (the same is true for a sharp crack). The loading rate was 0.1 mm/min for unnotched specimens and 0.01 mm/min for SENB specimens. Each kind of material was tested at least 5 times.

2.13. Simulation

The finite element method (FEM)-based simulation was implemented to capture the crack propagation process from macroscopic and microscopic scales [29–31]. The orthotropic constitutive model was utilized to describe mechanical behavior influenced by fibrils in a parallel arrangement. Cohesive zone model was adopted since the fracture mechanism mainly manifested as matrix debonding and brittle fracture of fibers. The fracture energy is identified by fracture test results. For the macroscopic model, the aim of simulation is to capture the main crack deflection and the laminar crack as the main crack propagated. The specimen in three-point bending test was modeled as a multilayer structure. For microscopic models, the aim of simulation is to explain the macroscopic fracture behavior from the scale of nanocrystalline. A brick-like structure was modeled, each brick represented a nanocrystalline with the size of 1 mm × 0.2 mm × 0.2 mm. The interfacial slip, debonding and brittle fracture along the fiber direction between bricks were described by cohesive behavior.

2.14. Calculation of fracture toughness $\boldsymbol{K_{JC}}$ and the crack extension $\Delta \boldsymbol{a}$ resistance curve

All test results are in accordance with ASTM standards.

1) K_{ic} is calculated by the following equations [8–10].

$$x = \frac{a}{W} \quad \text{(eq. 1)}$$

$$K_{ic} = \frac{P_{IC} S}{B W^{3/2}} f(x) \quad \text{(eq. 2)}$$

$$f(x) = \frac{3(x)^{1/2}[1.99 - x(1-x)(2.15 - 3.93x + x^2)]}{2(1+2x)(1-x)^{3/2}} \quad \text{(eq. 3)}$$

where P_{IC} is the maximum load before crack initiation, *S* is the span, *B* is the width, *W* is the thickness, and the a is the initial notch depth of the sample. *x* is a fixed value that is related to a *a* and *W*.

2) Crack length was recursively calculated as follows.

The single-edge notched beam sample will undergo a crack propagation process by the three-point bending test. Combined with SEM morphologies of crack propagation distance, the equivalent relationship between flexibility and crack length was used to calculate the crack propagation length for toughness analysis.

$$a_n = a_{n-1} + \frac{W - a_{n-1}}{2}\frac{(C_n - C_{n-1})}{Cn} \quad \text{(eq. 4)}$$

$$C_n = d_n / f_n \quad \text{(eq. 5)}$$

$$\Delta a = a_n - a \quad \text{(eq. 6)}$$

where a_n is the crack length, d_n is the displacement, and f_n is the force (N) at each point after crack initiation. C is the compliance calculated at the n and n-1 step respectively. Δa is the crack extension length.

3) The calculation for the relationship between K_{jc} and Δa.

J-integral versus crack extension was calculated by the contributions of elastic and plastic components and described as follows.

$$K_{JC} = \sqrt{(J_e + J_p)E'} \quad \text{(eq. 7)}$$

where.

J_e = elastic component of K_{ic},
J_p = plastic component of K_{jc},

$$E' = E / (1 - \nu^2) \quad \text{(eq. 8)}$$

where E is the flexural modulus of composite materials calculated by the three-point bend test.

$$E = \frac{\Delta S_{stress}}{\Delta S'_{Strain}} \quad \text{(eq. 9)}$$

where ΔS_{stress} and $\Delta S'_{Strain}$ stand the difference values at elastic stage of stress and strain curves.

$$J_e = \frac{{K_{ic}}^2}{E'} \quad \text{(eq. 10)}$$

$$J_p = \frac{2A_p}{Bb} \quad \text{(eq. 11)}$$

where A_p represents the plastic area under the load-displacement curve, B is the specimen lateral dimension, and b is the un-cracked ligament ($b = W - a$).

2.15. In vitro cytocompatibility of ACB

The *in vitro* cytocompatibility of the ACB was evaluated by cell culture of Sprague-Dawley rat BMSCs on the surfaces of ACB. First, ACB was washed by PBS and sterilized. The cells were then seeded at a density of 1×10^4 cells/sample on the ACB surfaces and cultured in a DMEM growth medium containing 10% fetal bovine serum and 1% penicillin-streptomycin in an incubator with 5% CO_2 at 37 °C.

For Live/Dead staining, the staining working solution (2 μM Calcein-AM; 4.5 μM PI) was prepared as follows. Solution A (2 mM, Calcein-AM (Yeasen, Cat No. 40747ES76; CO, China)) and solution B (1.5 mM, Propidium iodide, PI (Yeasen, Cat No. 40747ES80; CO, China)) were equilibrated at room temperature for 30 min before use. Add 15 μL of PI solution and 5 μL of Calcein-AM solution to 5 mL PBS solution, vortex and mix well, obtaining the staining working solution. Wash the cells with PBS to remove as much active esterase as possible from the culture. Add an adequate volume of the staining solution to ensure the monolayer of cells is fully covered, and incubate at room temperature for a duration of 30–45 min. Fluorescence microscopy was performed within 1 h.

To evaluate the cell morphologies after 5 days of culture, BMSCs were fixed with 4% paraformaldehyde in PBS and stained with rhodamine-phalloidin (1:300; Cat No. PHDR1; Cytoskeleton, Denver, CO, USA) for F-actin and SYTOX green (Thermo, Cat No. S7020; CO, USA) for nucleic acid and visualized through a laser scanning confocal microscope (LSCM, Zeiss LSM710, Germany).

Cell proliferation was measured *via* Cell Counting Kit-8 (CCK-8, Dojindo, Japan). The BMSCs were seeded on the samples in 48-well cell culture plates at a concentration of 1×10^4 per well and examined at 1 d, 3 d, and 5 d after cell seeding. The culture plate was used as a control. The quantitative values of OD at the wavelength of 450 nm were obtained using a microplate reader (Molecular Devices Spectra Max M5). All the measurements at each time point were repeated three times.

2.16. Enzymatic degradation of ACB

The *in vitro* degradation study was carried out at 37 °C. The samples were placed individually in a centrifuge tube and immersed in 50 mL PBS buffer solution containing different concentrations of proteinase K (0.05 mg/mL, 0.1 mg/mL, 0.2 mg/mL). The buffer enzyme solution was replaced daily to maintain a high enzymatic activity. ACB incubated without enzymes in PBS solution were also evaluated as a control. At the different timepoints, the scaffolds were weighed to calculate the mass loss.

2.17. In vivo biocompatibility of ACB in a rat distal femur defect model

The animal experiment on rats was approved by the Tsinghua University Institutional Animal Care and Use Committee (IACUC) and followed the Guide for the Care and Use of Laboratory Animals according to the Chinese Ministry of Public Health and U.S. National Institutes of Health Guidelines.

A rat distal femur defect model was used to assess the *in vivo* biocompatibility and osteogenic ability of the samples. Total of 24 SD rats (10-week-old, male) were randomly divided into two experimental groups (Control and ACB). Before the operation process, the rats were intraperitoneally anesthetized with 2 % sodium pentobarbital (0.3 mL/100 g weight of rats). A 3-mm bone drill was utilized to create a 3 mm diameter and 4 mm deep bone defect in the distal femur plateau of rats. The ACB material blocks were then implanted into the defects. The scaffolds with surrounding bone tissues were taken at 4 w, 8 w, and 12 w postoperatively for Micro-CT imaging and histological staining. In the control group, no scaffold materials were implanted. This blank control group was evaluated concurrently with the ACB group to facilitate a comparative analysis.

2.18. Histological staining and assessments of regenerated bone

The distal femur defect samples harvested at 4 w, 8 w, and 12 w weeks after surgery were fixed with 4% formaldehyde for 24 h and decalcified with 10% ethylenediaminetetraacetic acid (EDTA) for 4 months. After gradient dehydration, the samples were embedded in paraffin and cut into 4-μm-thickness sections using microtomes along sagittal slices direction close to the center of each implant (Leica RM2234, Germany).

2.19. Immunohistochemistry (IHC) staining

The OCN and CD31 IHC staining was performed to assess the osteogenesis and angiogenesis within 6 weeks. Briefly, the process followed the protocol of the Histostain-SP (Streptavidin-Peroxidase) kit (Shanghai Yaji Biotechnology Co., LTD.). After being blocked with goat serum for 30 min at 37 °C, tissue sections were incubated overnight at 4 °C with anti-osteocalcin rabbit pAb (1: 50; Cat. No. GB11233, Servicebio), and anti-CD31 rabbit pAb (1:50; Cat. No. GB113151,

Servicebio). Then, the secondary antibody and horseradish peroxidase streptavidin were added to the slices for 30 min at 37 °C. The sections were incubated by 3,3′-diaminobenzidine (DAB) as a chromogen substrate and counterstained with hematoxylin for 3 min at room temperature. Finally, the slides were dehydrated with the graded ethanol, transparent with xylene and mounted by neutral gum. The Image J software was utilized to measure the positive IHC staining region. The average values from each group were used for statistical analysis. The protein expression was semi-quantitatively calculated and classified based on the IHC staining areas.

2.20. Statistical analysis

All results are presented as the mean ± standard deviation. For *in vitro* studies, each experiment was conducted at least three times independently. The normality test was performed using the Kolmogorov-Smirnov test in SPSS (v.23.0; IBM Corp., Armonk, NY, USA). Statistical analysis of normally distributed data was carried out using independent t-tests or one-way analysis of variance (ANOVA). Differences were considered statistically significant when $p < 0.05$, shown as *; $p < 0.01$, shown as **; $p < 0.001$, shown as ***.

3. Results and discussions

3.1. Fabrication and physiochemical characterizations of the ACB

A cascade of continuous fabrication processes was successfully conducted to create a mineralized collagen-based lamellated compact bone analog, referred to as ACB (Fig. 1). The initial step involves synthesizing MC microfibrils through a previously reported *in vitro* biomimetic mineralization process. This process involves the combination of collagen molecules with Ca^{2+}/PO_4^{3-} ions, which regulate the nucleation and growth of CaP minerals on specific sites of the collagen microfibril template (Fig. 1A, Fig. S1, and Fig. S2). TEM images in Fig. S1 depict the characteristic nanoscale morphologies of MC microfibrils. Following the initial stage of mineralization (within one day), amorphous calcium phosphate nucleates along the collagen microfibrils and subsequently transforms into crystalline nHAp, exhibiting typical (002) and (211) SAED patterns. This process results in the formation of uniform MC microfibrils with an average diameter of 8–9 nm (Fig. S1E). SEM imaging showed the mineralized collagen microfibrils maintain their stable fibrous structure after freeze-drying (Fig. S2). Furthermore, EDS spectroscopy results reveal a uniform elemental distribution in the MC microfibril, with an atomic ratio of Ca/P approximately 1.52 (Figs. S1C–D). Due to the mild process of biomimetic mineralization that occurs under ambient conditions in aqueous environments, it is difficult to achieve the theoretical value of perfect crystal crystallinity for hydroxyapatite minerals. XPS results confirm the presence of Ca and P elements, and the shift in O 1s binding energy is likely due to chemical interactions between Ca^{2+} and O of -C=O during mineralization (Fig. S1F). In summary, the well-co-assembled MC microfibrils accurately mimic the crystallographic structure and composition of natural bone at the nanoscale level.

The prepared MC microfibrils were thoroughly mixed with PVA to form a slurry, which was subsequently transferred to a PDMS wedge for bidirectional freeze-casting (Fig. 1B and C). Simultaneously subjected to vertical and horizontal temperature gradients, the slurry began to freeze vertically away from the cold finger and horizontally along the surface of the PDMS wedge (Fig. S3). The growing ice crystals formed a lamellar structure at the microscale, causing the MC microfibril to align parallel to the slope of the PDMS wedge (*x*-axis) and become confined between the lamellae of ice crystals, resulting in a lamellar structure (Fig. 1C). Subsequently, the freeze-drying process yielded a bulk block consisting of MC microfibrils with a porous and lamellated structure. The schematic diagram was shown in Fig. 1D. The macroscopic morphology of the wedge-shaped porous block after freeze-drying was shown in Fig. 2A. The micro-CT morphology revealed the presence of parallel lamellar structure in the freeze-dried sample (Fig. S4). Finally, the application of high pressure led to the formation of the ACB bulk (Fig. 1E), which exhibited a striking resemblance to natural cortical bone in terms of appearance (Fig. 2B).

The ACB can be easily scaled up for production and processed into desired shapes (Fig. 2C). The SEM images of the porous block and compact ACB were examined, as shown in Fig. 2D–F. The aligned

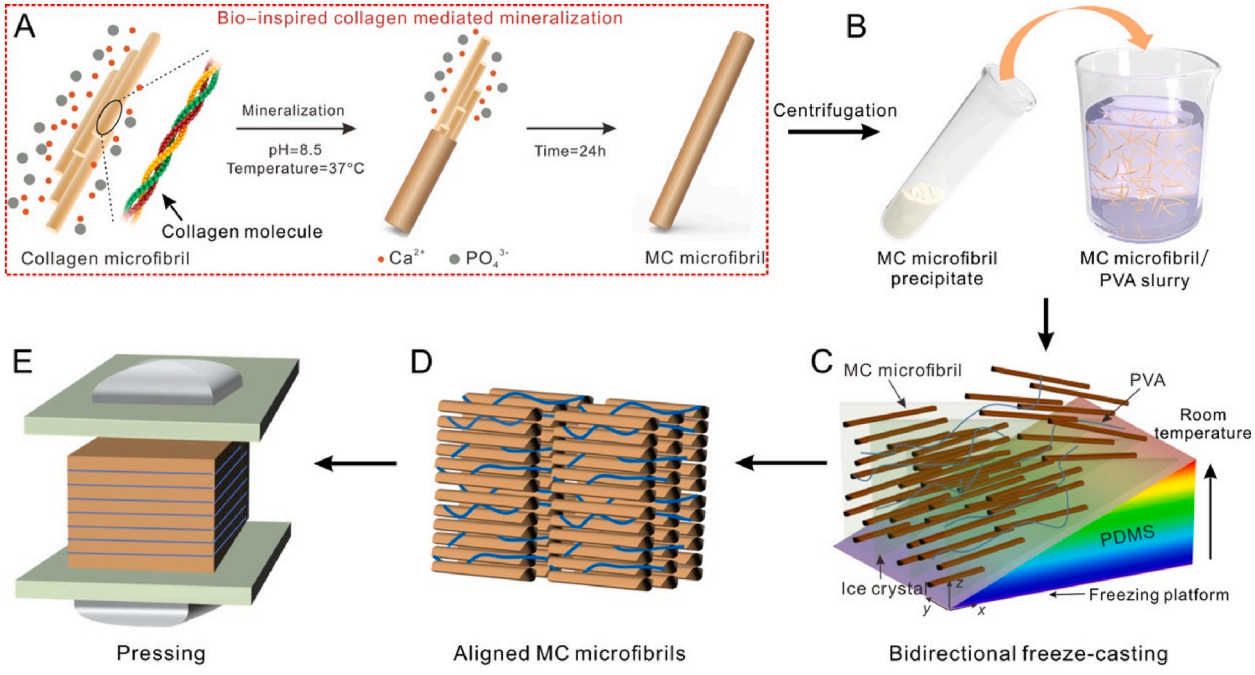

Fig. 1. Schematic illustration of artificial compact bone (ACB) fabrication. A, Collagen-mediated calcium phosphate mineralization process. B, Precipitate of MC microfibrils obtained after centrifugation and preparation of MC microfibril/PVA slurry. C, Preparation of aligned MC microfibrils by bidirectional freeze-casting. D, Aligned MC microfibril lamellae. E, Bulk ACB formation *via* pressure-driven fusion process.

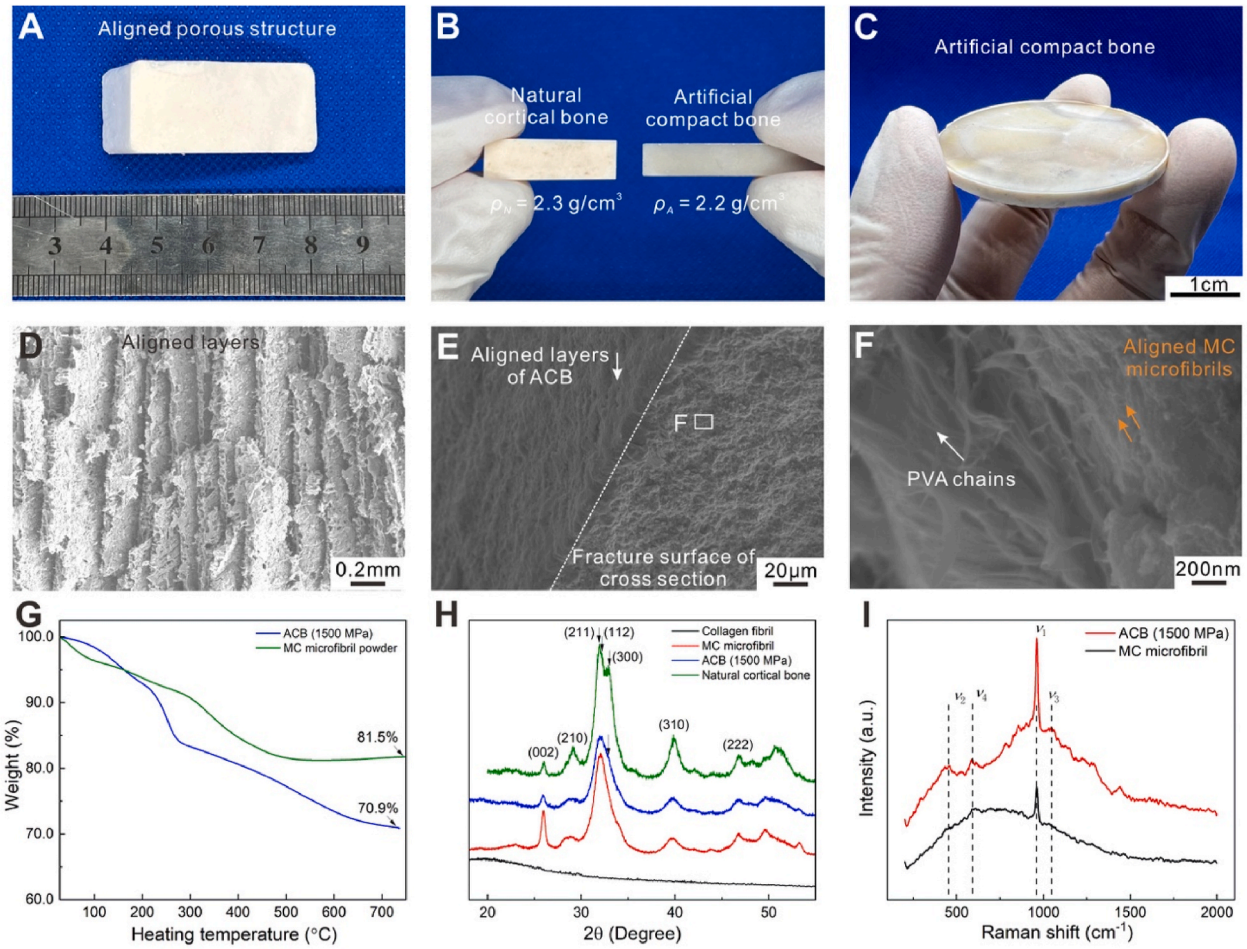

Fig. 2. Morphologies and physiochemical properties of ACB bulk. A, Aligned porous mineralized collagen-based bulk. B, The appearance of ACB resembling natural cortical bone. C, ACB can be processed into desired shapes. D, The aligned lamellar structure in the porous block. E, Aligned layers of ACB bulk. F, Aligned MC microfibrils and PVA. G, TGA analysis of ACB and MC microfibril powder. H, XRD spectra. I, Raman spectra, showing variations of peak intensities at 432 cm^{-1} (PO_4^{3-} ν_2), 593 cm^{-1} (PO_4^{3-} ν_4), 962 cm^{-1} (PO_4^{3-} ν_1), and 1028 cm^{-1} (PO_4^{3-} ν_3) between ACB and MC microfibril.

lamellar structure in the porous block is clearly observed (Fig. 2D). After compression, the ACB maintained the lamellar structure with MC microfibrils in a parallel arrangement pattern (Fig. 2E and F). Additionally, the density of ACB was approximately 2.2 g/cm^3, which is almost the same as that of natural cortical bone (~1.8–2.3 g/cm^3). This similarity can be attributed to the high mineral content (70.9%) and compact structure of ACB, which resembles that of natural bone (Fig. 2G). The XRD spectra confirmed the presence of hydroxyapatite minerals in the ACB (Fig. 2H). The Raman examination showed similar spectra for ACB and MC microfibrils, indicating that the pressure-driven fusion did not alter their chemical structures, displaying crystal structure peaks that are consistent with the structure of bone (Fig. 2I). In summary, these results indicate that the ACB exhibits similar features, including density, inorganic content, crystal structure, and composition, to natural bone. Another, the microscopic morphology of RCB is shown in Fig. S5. The MC microfibrils maintain an alignment structure within multiple sub-millimeter domains.

To further validate the hierarchical assembly of mineralized collagen, we examined the microstructures of the ACB across multiple length scales, ranging from the nano to macro levels. Micro-CT scanning was employed to visualize the compact and layered features of ACB in three dimensions under X-ray imaging (Fig. 3A). SEM images of the horizonal cross-sections (x-y plane in Fig. 1C) revealed the presence of aligned lamellae at the microscale and aligned MC microfibrils at the nanoscale (Fig. 3B–C). TEM images with SAED and FFT patterns were obtained from the horizontal cross-section of ACB (x-y plane in Fig. 1C) fabricated by FIB thin-cut, as shown in Fig. 3D–F. The MC microfibrils were arranged in a nearly parallel manner. The SAED and FFT patterns revealed the characteristic (002) preferred orientation of hydroxyapatite nanocrystals along the longitudinal direction of collagen microfibrils (Fig. 3D–E), suggesting the biomimetic co-assembly of collagen and nHAp at the nanoscale. The high-resolution TEM images revealed the presence of aligned molecules with a diameter of 1.5 nm, which was consistent with the theoretical value of collagen triple-helical molecules (Fig. 3F). And a fine-striated pattern with a period of ~3.46 Å is expected to correspond to the (002) crystal plane spacing of nHAp of MC microfibrils. Furthermore, the high-resolution TEM images of the vertical cross-sections (y-z plane in Fig. 1C) revealed the presence of identical crystal structures of nHAp, indicating the crystallographic consistency of the arrangement of nHAp grains. The white dashed lines represent the vertically aligned structure of assembled mineralized collagen microfibrils. The FFT results indicate the presence of a (001) diffraction pattern (Figs. S6A–C). Additionally, the STEM image of the MC microfibril obtained using the high-angle annular dark field (HAADF) mode, along with the corresponding EDS mapping images of Ca, P, and C elements, also exhibited a nearly aligned structure (Figs. S7A–C). The atomic-resolution HAADF images obtained from TEM revealed the arrangement of Ca atoms in the nHAp of aligned MC microfibrils, which indicated the mutually parallel morphology of MC microfibril in ACB (Figs. S8A–C).

Besides the bidirectional freeze-casting process that controls the alignment of MC microfibrils, the pressure-driven fusion process is

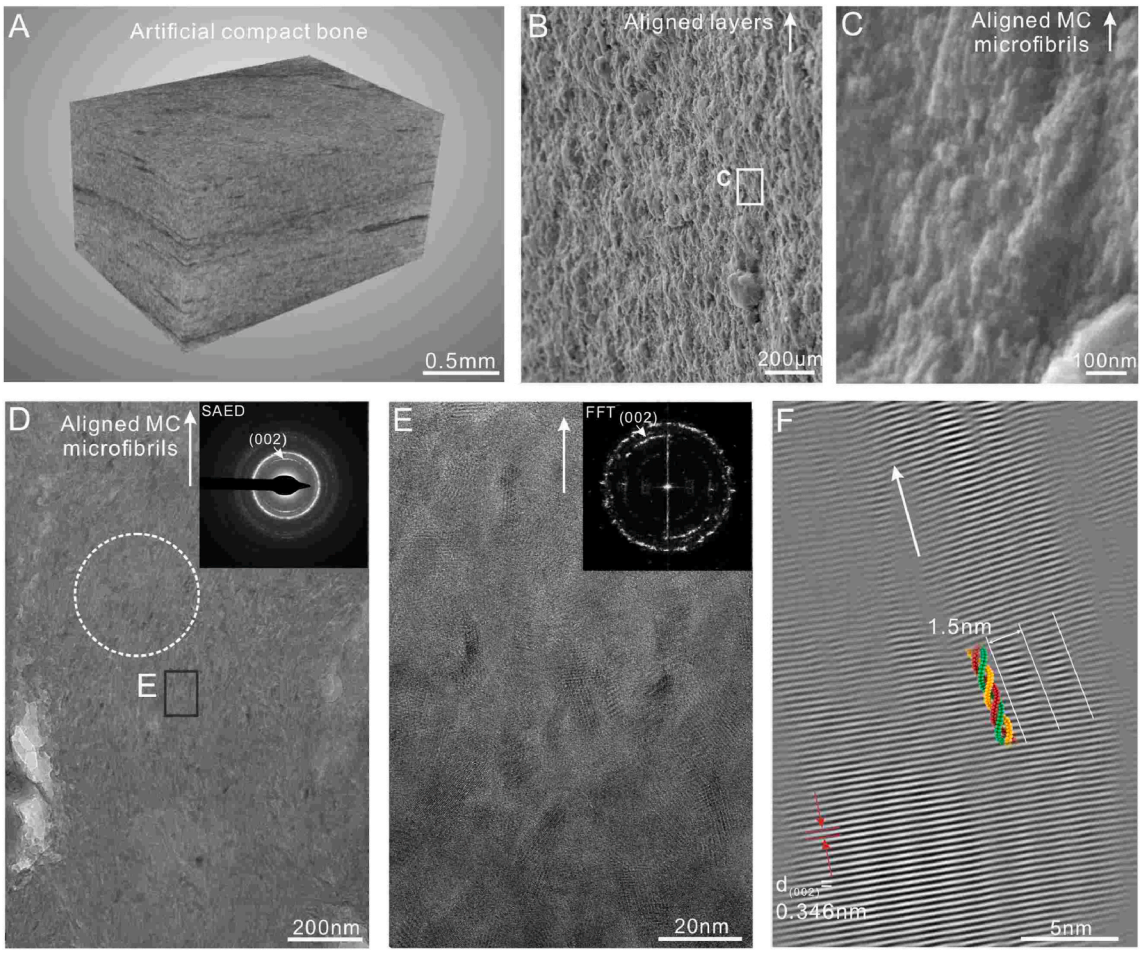

Fig. 3. Hierarchical and highly ordered structure of artificial compact bone. A, Micro-CT morphology of ACB. SEM morphologies of aligned lamellated structure (B) and aligned MC microfibrils (C). D, TEM images and SAED patterns. E, Partial enlarged images and FFT patterns. White arrow stands for the orientation of MC microfibril. The corresponding SAED and FFT patterns revealed the characteristic (002) preferred orientation of hydroxyapatite nanocrystals along the longitudinal direction of collagen microfibrils. F, High-resolution TEM images of aligned MC microfibrils, revealing the presence of aligned collagen molecules (~1.5 nm in diameter) and a fine striated pattern with a period of ~3.46 Å, which is expected to correspond to the (002) crystal plane spacing of nHAp.

crucial for achieving a highly compact structure. Under high compression, the inorganic apatite minerals in the MC microfibrils undergo fusion and contribute to the stability of the structure. Our previous study suggested that the fusion and transformation of low-crystallinity inorganic phases within the MC fibrils contribute to the formation of a compact structure under pressure [22]. To further confirm the occurrence of fusion phenomena, we conducted XPS, XRD, FTIR, and TGA analyses on the ACB samples obtained under various pressures. It should be noted that there is an increase in the intensity of the O 1s, Ca 2p, and P 2p peaks, as well as subtle shifts in the binding energy of Ca and P in the XPS spectra, which may indicate the fusion of calcium phosphate crystals and an increase in crystallinity (Fig. S9). The TGA tests revealed that the ACB specimens obtained under different pressures of 1 MPa, 200 MPa, and 1500 MPa had almost the same nHAp content (~70%), but exhibited different weight-loss rates between 400 and 700 °C, confirming an increase in the crystallinity/maturation of nHAp in ACB with increasing fusion pressure (Figs. S10A–B). Furthermore, the FTIR and XRD spectra, which are capable of reflecting the crystallinity and crystallographic structure of nHAp, yielded consistent conclusions with the aforementioned measurements (Fig. S11). Notably, the significant increase in the intensity of the 002-peak in ACB ($P = 1500$ MPa) suggests that the external high pressure may induce a more pronounced preferential orientation of these "deck of cards" crystals. More than that, the addition of PVA polymer during the bidirectional freeze-casting process also plays a crucial role in the formation of ACB. PVA was utilized to prevent the rapid precipitation of MC microfibrils during the entire freeze-casting process, thereby promoting the three-dimensional orientation and arrangement of MC microfibrils with bidirectional temperature gradients. In the absence of PVA, the MC microfibrils tended to sediment, resulting in a lack of uniform directional arrangement and disintegrated feature. The TGA results indicated that the PVA content in the ACB is approximately 13%.

3.2. Mechanical properties of ACB

Given the similar composition and hierarchical structure between ACB and natural cortical bone, it is expected that the mechanical properties, such as strength, stiffness, and toughness, would be enhanced. Due to the anisotropic microstructure of ACB, the mechanical properties were assessed along three distinct orientations: antiplane (with the load applied perpendicular to the lamellar structure), in-plane PD (with the load applied parallel to the lamellar structure but perpendicular to the MC microfibrils), and in-plane LD (with the load applied parallel to both the lamellar structure and the MC microfibril) (Fig. 4A). Additionally, the RCB was also examined for comparison.

We evaluated the mechanical performance of ACB and RCB using both nanoindentation to measure stiffness and hardness, and the three-point bending test to measure flexural modulus, strength, and toughness in both antiplane and in-plane directions (Fig. 4B–C, Fig. S12, and Fig. S13). The biomimetic compact bone bulks exhibited similar density

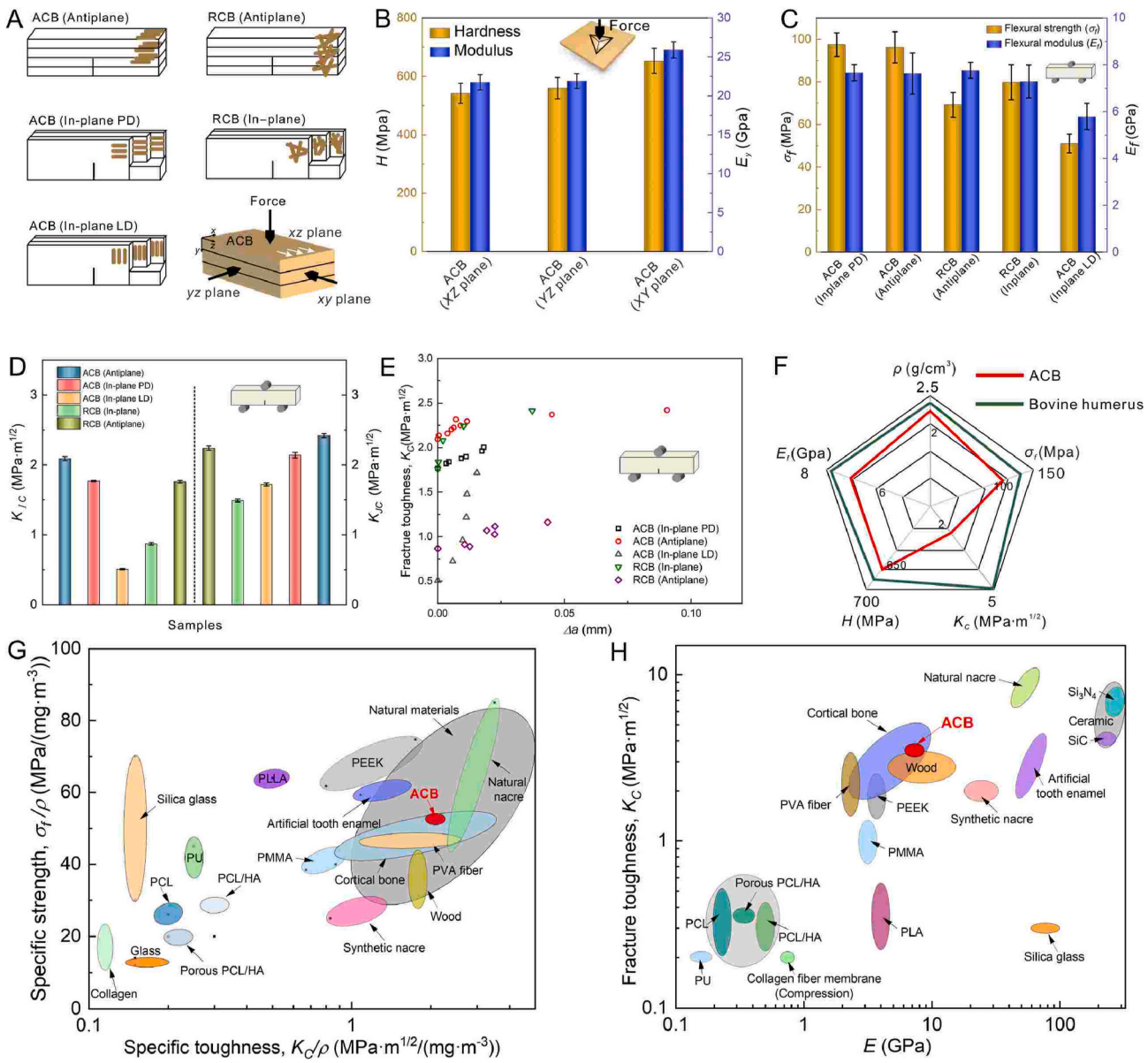

Fig. 4. Mechanical properties of artificial compact bone. A, Schematic illustration for three-point bending and nanoindentation test in different directions or planes. B, Statistics for hardness (H) and modulus (E_y) of ACB in different planes by nanoindentation test. C, Statistics and comparison of flexural strength (σ_f) and stiffness (E_f) of the ACB and RCB. D, Fracture toughness for crack initiation (K_{IC}) and stable crack propagation (K_{JC}) of the ACB and RCB. E, Crack-resistance curves (R-curves) showing the resistance to fracture in terms of the stress intensity, K_{JC}, as a function of crack extension, Δa, for the ACB and RCB bulks. F, Mechanical performance of ACB compared to natural cortical bone. G-H, Comparison of mechanical properties of ACB with natural materials and some composites. G, Ashby diagram of the fracture toughness of ACB compared with a wide range of natural structural materials and biomaterials as a function of their stiffness. H, Ashby diagram of specific strength *vs.* toughness for ACB compared with a range of synthetic and natural materials.

(~2.2 g/cm^3), surface hardness (H, 653.0 ± 43.1 MPa in x-y plane), and Young's modulus (E_y, 25.9 ± 1.1 GPa in x-y plane) to natural cortical bone (Table S1). This similarity can be attributed to the high mineral content and compactness of ACB under high compressive pressure (Fig. 4B). Additionally, the ACB demonstrated good flexural performance during the three-point bending test (Movie 1). The ACB bulk exhibited ultimate flexural strengths of 97.5 ± 5.6 MPa and 96.2 ± 7.3 MPa, along with moduli of 7.66 ± 0.35 GPa and 7.63 ± 0.88 GPa, in the antiplane and in-plane PD directions, respectively. In contrast, the RCB exhibited ultimate flexural strengths of 79.8 ± 8.2 MPa (in-plane) and 69.2 ± 5.8 MPa (antiplane), along with flexural moduli of 7.29 ± 0.70 GPa (antiplane) and 7.77 ± 0.34 GPa (in-plane), respectively (Fig. 4C). The significant difference in flexural strengths between the ACB and RCB indicated the important role of aligned MC microfibrils in enhancing flexural strength. However, the difference in their flexural moduli was not as significant, as the modulus was predominantly contributed by inorganic minerals.

Fracture toughness was evaluated through single-edge notched beam tests. Fig. S14 showed the typical load-displacement curves obtained from SENB tests. The initial fracture toughness (K_{IC}) of ACB in in-plane PD (1.77 ± 0.03 MPa m$^{1/2}$), antiplane (2.09 ± 0.01 MPa m$^{1/2}$), and in-plane LD (0.51 ± 0.01 MPa m$^{1/2}$), as well as RCB in antiplane (1.76 ± 0.02 MPa m$^{1/2}$) and in-plane (0.87 ± 0.02 MPa m$^{1/2}$), indicated that ACB and RCB exhibited good resistance to initial crack propagation during deformation (Fig. 4D and Table S2). The maximum fracture toughness (K_{JC}) of both ACB and RCB shown by J-R curves exhibited a clear increasing trend, indicating the effectiveness of the multilayer structure in preventing crack propagation (Fig. 4E). The fracture

toughness of ACB in different loading directions, such as antiplane (2.42 ± 0.03 MPa $m^{1/2}$), in-plane PD (2.14 ± 0.04 MPa $m^{1/2}$) and in-plane LD (1.72 ± 0.02 MPa $m^{1/2}$), as well as RCB in antiplane (2.24 ± 0.03 MPa $m^{1/2}$) and in-plane (1.49 ± 0.02 MPa $m^{1/2}$), approached a lower value compared to that of natural cortical bone (3–6 MPa $m^{1/2}$). However, other mechanical properties including hardness, flexural modulus and strength were comparable to those of natural cortical bone (Fig. 4F) [18]. Fig. 4G illustrates the relationship between the flexural modulus (E_f) of ACB and its fracture toughness (K_C), demonstrating the remarkable potential of synthetic bulk ACB to match natural materials and maintain toughness despite increased stiffness. Moreover, the ACB exhibits superior specific strength (σ_f/ρ) and specific toughness (K_C/ρ) compared to some typical synthetic biomaterials (Fig. 4H and Table S3). These exceptional properties primarily arise from the hierarchical organization and aligned MC microfibrils-based lamellar structure.

Human cortical bone is an excellent example of achieving both exceptional strength and toughness through intrinsic and extrinsic toughening mechanisms. Intrinsic toughening originates from the fibrillar sliding mechanism occurring at length scales ranging from tens to hundreds of nanometers, which are closely related to the MC fibrils in bone. However, the primary contributor to bone toughness is extrinsic, resulting from crack bridging and deflection when a propagating crack encounters the highly mineralized interfaces within the lamellar or osteonal structures at the micrometer or millimeter scale [32]. By imitating the hierarchical structures found in natural bone, the block ACB should exhibit the potential synergistic effects of both intrinsic and extrinsic toughening mechanisms. Therefore, the crack propagation behaviors and fracture surface morphologies of ACB (antiplane and in-plane PD) were examined after the SENB test (Fig. 5A–H, Fig. S15, and Fig. S16). The crack in the bulk ACB initiates from the notch ahead of the crack tip and propagates along a rough path. Typical crack deflection/twists, micro-cracks, MC microfibril bridging, and crack branching were observed, which contributed to the excellent extrinsic toughening mechanism. Besides, the high-magnification morphologies of the nanoindentation impression showed crack deflection and jagged crack twists along the interfaces of MC microfibrils at the nanoscale, which indicates the toughening effect of MC microfibrils at the nanoscale level (Fig. 5I–K). The MC microfibrils that are composed of an elaborate assembly of collagen microfibrils and nHAp with a diameter of 8–9 nm, exhibit an important intrinsic toughening effect, involving fibril sliding, bending, and pull-out behaviors during the yielding stage. This underlying mechanism is derived from the slipping that occurs at the hydroxyapatite/collagen interface, which allows for a significant dissipation of energy and effectively enhances fracture resistance (Fig. 5H).

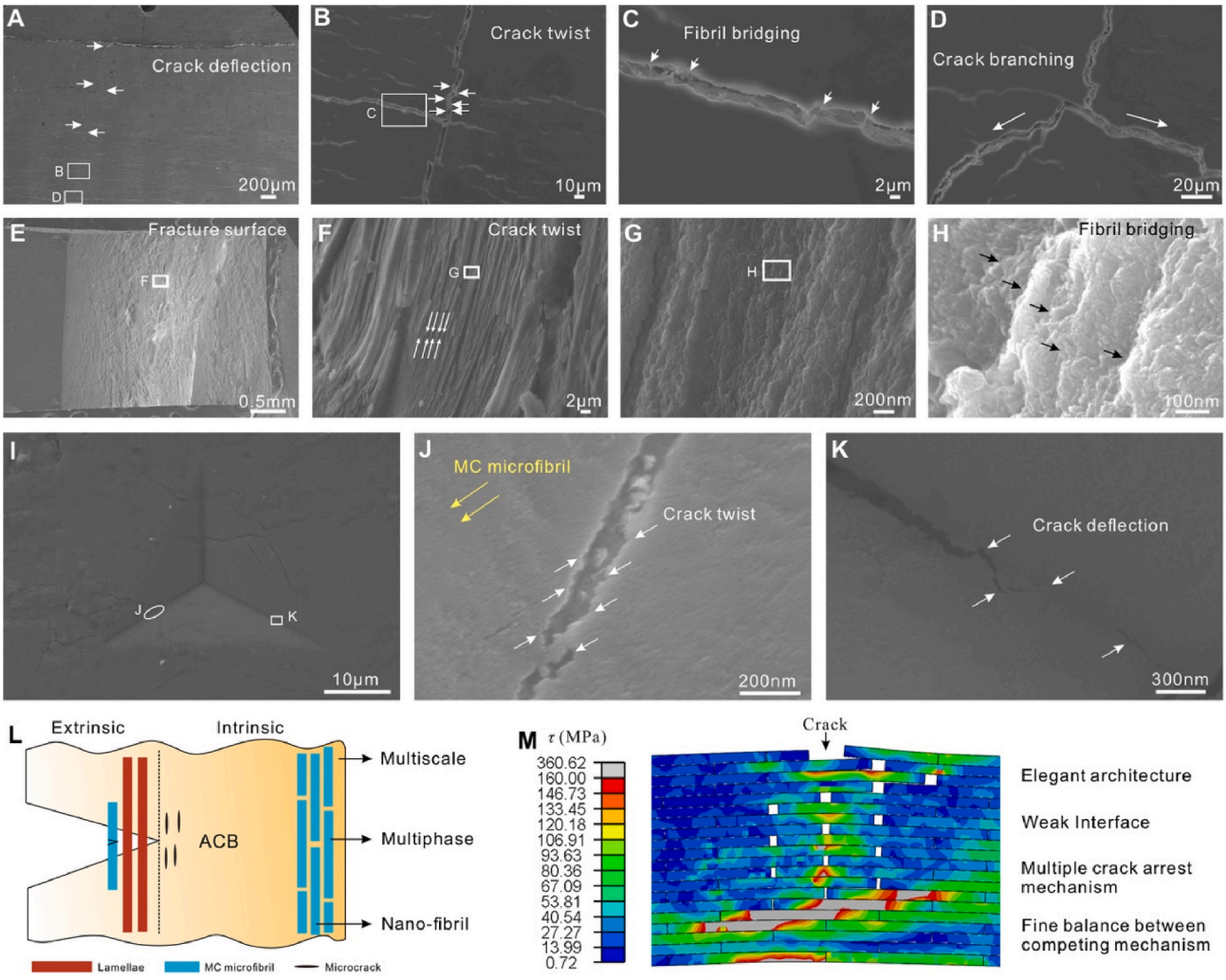

Fig. 5. The crack propagation behaviors and fracture surface morphologies after the SENB test. A, Crack propagation path with obvious crack deflections along the interlamellar interface in ACB (antiplane). B, Enlarged regions along the crack path show the crack twist, fibril bridging (C) and crack branching (D). E-H, Multilevel fracture surface morphologies. I, SEM images of the nanoindentation impression in ACB (*x*-*z* plane). J, Aligned MC microfibril crack twist. K, Crack deflection. L, Schematic plot of ACB with extrinsic and intrinsic toughening mechanism. M, Microcrack deflection and crack bridging near the crack tip by progressive interface failure *via* nonlinear finite element model simulation in sublayer.

In summary, we believe that the combination of the proposed intrinsic and extrinsic toughening mechanisms effectively redistributes and alleviates the high stresses that occur at multiple scales. The concurrent presence of multiscale, multiphase, and microfibril conditions ultimately gives rise to the observed increase in the R-curve in the artificial bulk bone (Fig. 5L).

Moreover, the nonlinear finite element modeling simulation demonstrated clear microcrack deflection near the crack tip through progressive interface failure, bending, and pull-out of the analog unit in a typical fibril/fibril alignment structure (Fig. 5M and Movie 2). Additionally, the macroscopic fracture simulation revealed the typical behaviors of crack deflection and interface branching (Fig. S17 and Movie 3). This pathway is consistent with the reinforcement and toughening of nanofibrils during the actual ACB fracture process. Therefore, we have summarized the characteristics of the bone-mimicking structure, including a multiscale and laminated structure with aligned nanofibers and multiple phases contributed to superior crack resistance through hierarchically elegant architecture, weak interfaces, crack arrest mechanism, and the simultaneous activation of multiple mechanisms that prevent crack propagation (Fig. 5L). However, it should be noted that the ACB is composed solely of aligned MC microfibrils, without the higher-level organization of MC fibers/bundles and rotated arrays found in natural bone. This should be the reason why the fracture toughness of ACB is not as good as that of natural bone, including the ALB we prepared previously.

3.3. *In vitro and in vivo biocompatibility of ACB*

Due to its high inorganic content, the ACB demonstrates excellent stability in PBS without any observable swelling (Movie 4). After being fully immersed for 7 days, the ACB maintained its mechanical strength, with a flexural strength of approximately 30.3 MPa, a flexural strain of around 60 %, and a flexural toughness of 5.33 ± 0.2 MPa $m^{1/2}$ (Fig. 6A–E). Furthermore, even after being continuously immersed for over a month, the ACB retains its mechanical performance. This significant plastic behavior can be attributed to the widened spacing between MC microfibers, which allows the polymer chains to become more flexible. Consequently, this leads to a decrease in strength, stiffness, and hardness, while simultaneously enhancing toughness and plasticity. Furthermore, we conducted an enzymatic degradation experiment of ACB using protease K. The *in vitro* degradation of the ACB is dependent on the dose of protease K, as shown in Fig. S18. The weight of the ACB decreased by approximately 5–6% during the 7-day degradation process. These results suggest that ACB exhibits slow biodegradation, which implies its potential for long-term stability *in vivo*.

To assess the cytocompatibility of ACB bulk *in vitro*, BMSCs were cultured on the surface of ACB to observe their adhesion, proliferation, and spreading behaviors (Fig. 6F–I). The Live/Dead staining result demonstrated that the majority of BMSCs remained viable and exhibited robust growth, as indicated by the absence of red-stained dead cells (Fig. 6F). Furthermore, the CCK-8 assay revealed that the cells cultured on ACB exhibited an excellent and stable proliferation rate comparable to the control group (Fig. 6I). Moreover, the SEM and LSCM images depicted the morphologies of BMSCs cultured on ACB, demonstrating favorable attachment and spreading behavior with a characteristic spindle-shaped morphology (Fig. 6G–H). Following 5 days of culture, the BMSCs exhibited rapid proliferation and reached confluence. The aforementioned results indicate that ACB exhibits excellent cytocompatibility for cell attachment and growth.

To evaluate the *in vivo* biocompatibility of the ACB bulk and its potential for bone repair, we employed a distal femur defect model. Cylindrical ACB scaffolds, with a diameter of 3 mm and a height of 4 mm, were machined to include two through-holes with a diameter of 0.8 mm and then inserted into bone defects of matching size (Fig. 6J). Bone tissues were harvested and analyzed at 4, 8, and 12 weeks post-surgery. In the control group, no significant bone regrowth was observed within the interior of defected region, with only a small amount of new bone tissue formed along the edges of the defect (Fig. 6K-M, middle figures). In the ACB group, the ACB with bone ingrowth into the holes and around the scaffold were evaluated using micro-CT imaging (Fig. 6K-M). The compact structure of ACB showed no obvious degradation within 12 weeks, indicating its long-term *in vivo* stability. At four weeks post-surgery, rapid new bone ingrowth was observed in the inner hole, demonstrating the excellent biocompatibility and osteoconductivity of ACB. As time progressed, more bone tissue regenerated around the entire scaffold, extending even to the surface of the bone tissue. Despite the lack of a significant degradation process, ACB exhibited excellent osteointegration with surrounding bone tissues. Considering the remarkably slow degradation rate of ACB and the absence of implants in the defect of the control group, it is inappropriate to calculate the volume of the whole defects. We examined the regions adjacent to the defect edge, extending 0.3 mm inward from the defect edge for assessing new bone formation. For the ACB group, the calculated bone volume/total volume (BV/TV), trabecular thickness (TbTh), and bone surface/bone volume (BS/BV) showed a gradual increase, while the trabecular spacing (TbSp) and average trabecular number (TbN) decreased over time within 12 weeks (Fig. 6N-R). These results indicate that ACB has good tissue compatibility and achieves successful postoperative repair. The new bone tissue exhibited exceptional osteointegration with the ACB scaffold, with no fibrous tissue at the interface, confirming ACB's excellent biocompatibility and potential osteogenic ability. In the control group, the statistical results of new bone formation show no significant increase from 4 w to 12 w post-surgery.

The regenerated bone tissues were further visualized by histological assessments. The typical morphologies of the H&E, and Masson's trichrome stained cross-sections at the time points of 4, 8, and 12 weeks were examined, respectively. For the H&E-stained images (Fig. 7A), the pink color of dense tissues indicated the newly formed bone tissue, marked by ★, which could be easily distinguished from the ACB scaffolds (the dense structure characterized as ■) and loose fibrous tissues (marked by ●). None of the bone defect specimens showed any signs of inflammation or infection induced by the ACB material (Fig. 7A, Fig. S19A). The ACB scaffold (0.8 mm hole) embedded in the distal femur defect provided a good bridge for cell migration, growth, and ECM deposition. According to the results of H&E and Masson trichrome staining, the ACB promoted bone invasion from the surrounding bone tissues and formed obvious neo-bone tissue structures along the surfaces of ACB (red arrows), and then gradually became mature (Fig. 7B, Fig. S19B). These results confirmed the excellent osteointegration capability of the ACB. In addition, the histological results showed that the ACB group had the higher bone regeneration rate with the faster vascularization, which was consistent with the Micro-CT results. In contrast, the defects in the control group had new bone formation only around the defect edges at 4, 8, and 12 weeks, while the interior was replaced by sparse fibrous tissue (marked by ●) without bone structure formation.

Furthermore, the immunohistochemical staining of OCN and CD31 was conducted to confirm the osteogenesis and angiogenesis surrounding the ACB. The presence of OCN-positive regions in the defect area was significantly more pronounced in the ACB group compared to the control group, suggesting the improved osteogenesis induced by ACB (Fig. 7C, Fig. S19C). In addition, newborn blood vessels were observed by immunostaining of CD31 marker (Fig. 7D, Fig. S19D). The statistical analysis revealed a significant increase of CD31-positive cells in the ACB group compared to the control groups, providing evidence for the enhanced angiogenesis process facilitated by ACB (Fig. 7F). Overall, the results suggest that ACB plays a significant role in promoting rapid vascularization and bone regeneration due to its exceptional mechanical properties and osteogenic/angiogenic activities.

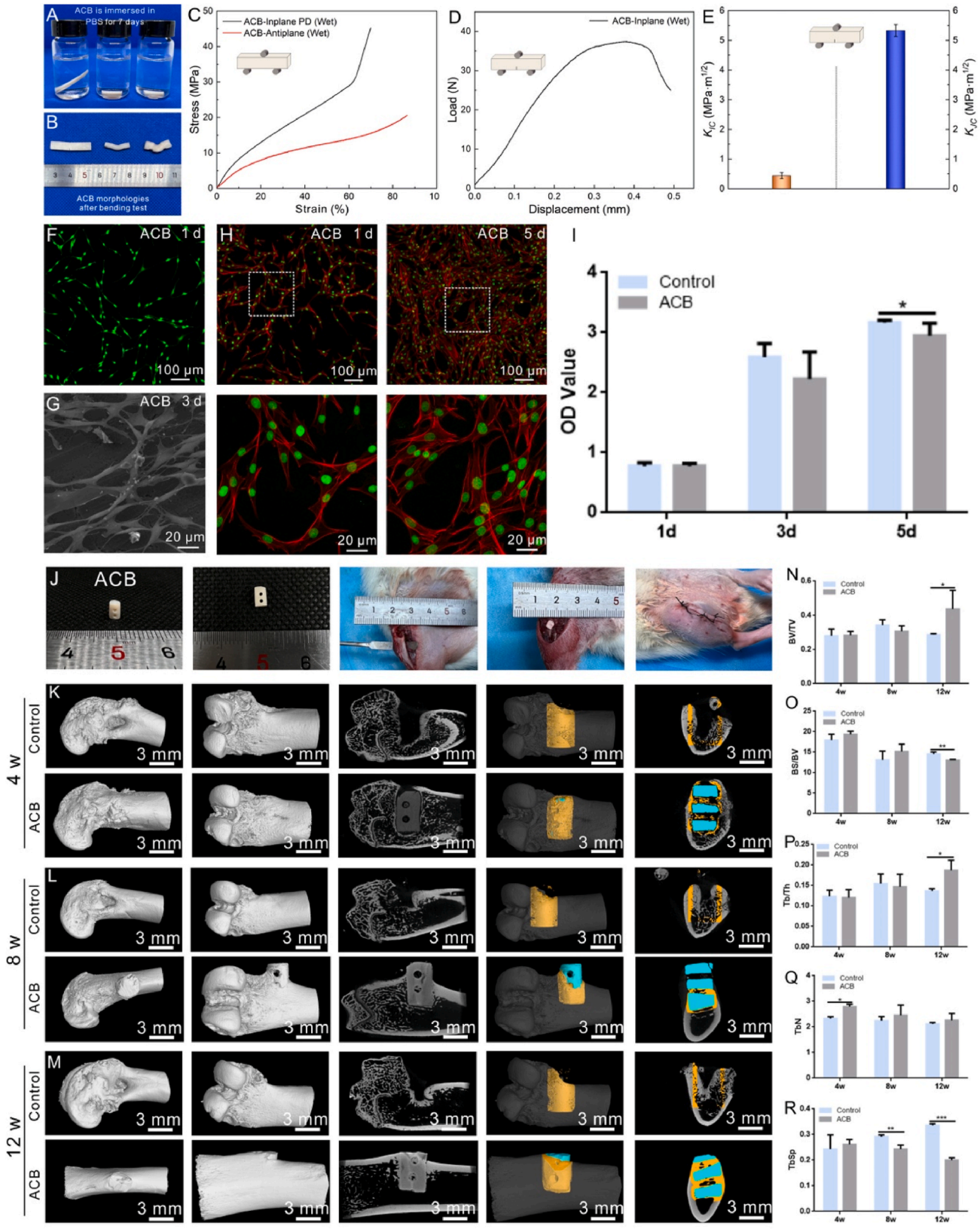

Fig. 6. The performance of ACB after being immersed in PBS and *in vitro/in vivo* biocompatibility. A, Appearance of ACB in PBS. B, Three-point bending tests and SENB tests for ACB (wet). C, Flexural strength and flexural strain curves for ACB (In-plane PD and Antiplane, wet). D, Load-displacement curves for ACB (in-plane PD, wet) by SENB test. E, Statistic of K_{IC} and K_{JC} for ACB (in-plane PD, wet). F, LIVE/DEAD staining of BMSCs cultured on ACB for 1 d. G, Corresponding SEM micrographs of BMSCs at 3 d. H, LSCM morphologies of the BMSCs on ACB after 1 d and 5 d of cell culture (rhodamine-phalloidin for F-actin in red and SYTOX-green for nucleic acid in green). I, Cell proliferation by CCK-8 assay. J, Surgical procedure for creating a distal femur defect model in rats. K-M, 3D reconstruction of Micro-CT imaging at 4 w, 8 w, and 12 w post-surgery of control and ACB group. N-R, The statistics of BV/TV, BS/BV, TbTh, TbN, and TbSp. n = 3. $^{*}P < 0.05$, $^{**}P < 0.01$, $^{***}P < 0.001$.

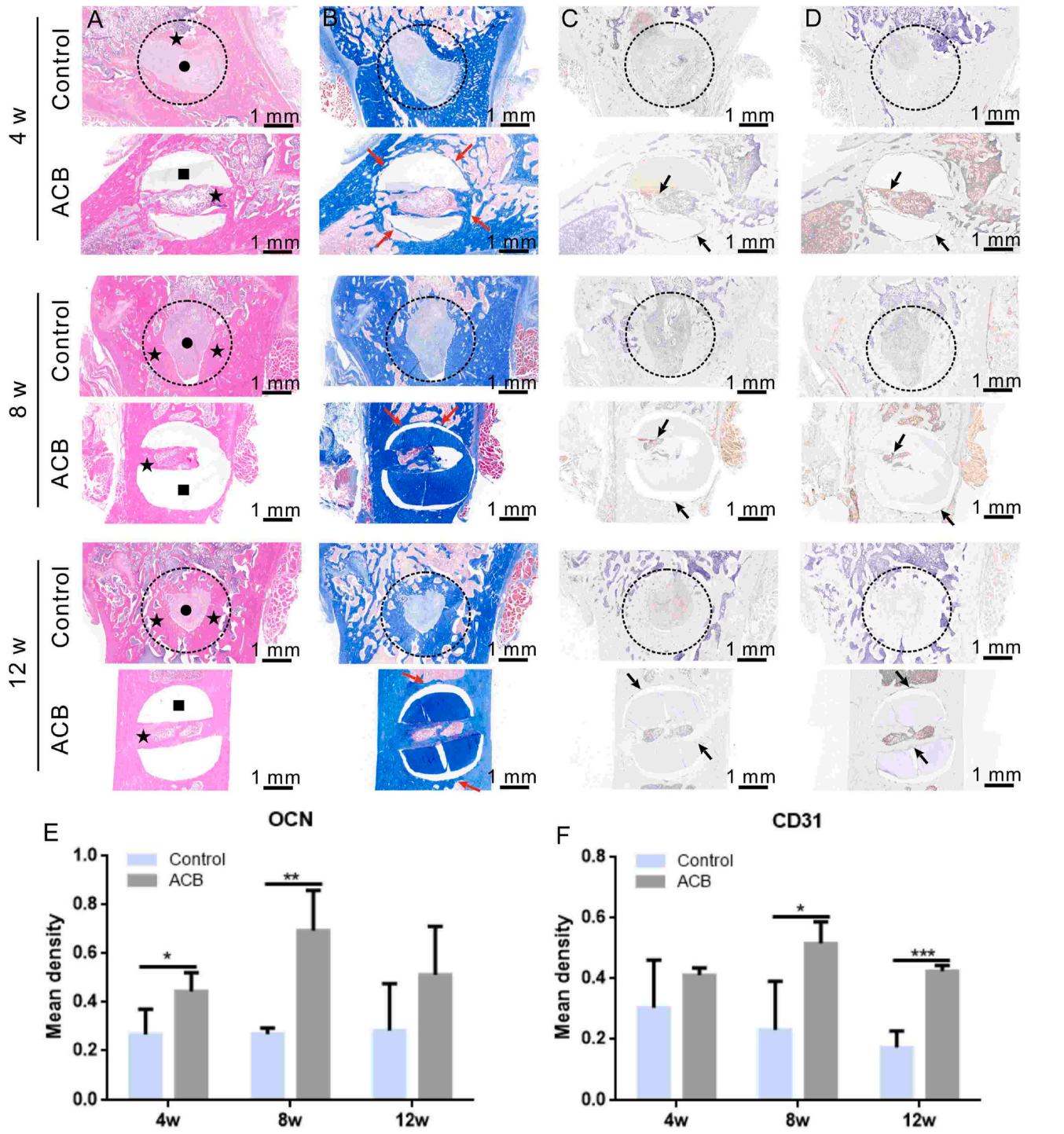

Fig. 7. Histological straining images of the regenerated tissues at 4 w, 8 w, and 12 w post-surgery. A, H&E straining images. B, Masson trichrome staining images (Red arrows: neo-bone). '■' stands for ACB scaffold materials, '●' stands for loose fibrous tissues, and '★' describes the new bone tissues. C, OCN staining images (Black arrows: neo-bone). D, CD 31 staining images (Black arrows: neo-bone). E and F, The IHC staining for OCN, and CD 31 at defect area and quantitative analysis. n = 3. $^{*}P < 0.05$, $^{**}P < 0.01$, $^{***}P < 0.001$.

3.4. Discussions

In this study, the oriented arrangement of MC microfibrils across a wide range of scales, from micrometers to macroscopic levels, was achieved through a bidirectional freeze-casting process. As a result, a layered alignment composed of oriented MC microfibrils was formed. By combining pressure fusion, we successfully fabricated an artificial compact bone structure that closely resembles natural bone in terms of composition and structure. The ACB material demonstrates not only a composition and content that closely resemble natural bone, but also a layered structure and cross-scale ordered assembly of MC microfibrils that closely resemble those found in natural bone. The method utilized in this study enables convenient and efficient fabrication, facilitating scalable production. Furthermore, the prepared ACB materials exhibit comprehensive properties that are comparable to those of natural bone, including strength, hardness, modulus, density, and bioactivity.

Similar to the previously prepared ALB, ACB is mainly composed of MC microfibrils serving as assembled units for hierarchical organization.

Furthermore, both materials exhibit in-situ co-assembly of collagen and hydroxyapatite at the nanoscale, along with a lamellar structure at the micrometer scale. Consequently, both ACB and ALB exhibit excellent resistance to bending and crack propagation. In contrast, ALB differs by having a 30° incremental angle between adjacent lamellar layers, resulting in a more biomimetic resemblance to natural lamellar bone. The MC microfibrils within the parallel lamellae structure of ACB do not display incremental rotation angles between layers. Consequently, ACB may have lower toughness in a specific direction compared to ALB. Nevertheless, the electrospinning process used for ALB preparation imposes limitations on both the mineral content of ALB and the chemical crosslinking process. Therefore, we found that ALB is prone to rapid swelling and degradation *in vivo*. In this study, we have successfully addressed the mineral content limitation issue of ALB materials and synthesized an ACB material by bidirectional freezing technique that closely resembles the actual bone mineral content. Thus, the ACB exhibits comparable density and hardness to natural bones. The bidirectional freezing technique could effectively drive the assembly and alignment of small building blocks into lamellar structure. Here, we combined the bidirectional freezing technique with molecular self-assembly of mineralized collagen and pressure-driven fusion for the first time to produce a macroscopic bulk artificial compact bone material.

More than that, the contribution of bidirectional freezing technique for ACB preparation is not limited to mineral content but also includes process optimization, economic benefits enhancement, and potential clinical applications. Compared to electrospinning technology, the bidirectional freezing process enables efficient, rapid, scalable production while conserving energy. The process eliminates concerns regarding environmental pollution caused by the volatile organic solvents used in the electrospinning process, as well as the risks associated with high voltages.

Furthermore, our previous research and this study have demonstrated that the inorganic minerals play a significant role in pressure-driven fusion. As the pressure increases, crystal fusion and crystallinity increase, facilitating the densification and interlayer bonding of the material as a whole. Due to its higher mineralization content, ACB exhibits greater stability than ALB under equivalent pressure. *In vitro* swelling and *in vivo* implantation experiments demonstrated that ACB exhibited minimal swelling, high stability, and relatively slow degradation in an aqueous environment. Notably, ACB did not experience collapse degradation and became more pliable. However, maintaining the long-term effectiveness of ALB becomes challenging when it is implanted for repair in the body due to its degradation rate surpassing the rate of bone healing. Additionally, the densification was also promoted through pressure-fusion at 80 °C. Heating is beneficial for removing air and reducing pore size, even though ACB can be obtained through pressure-fusion at room temperature. Given that the denaturation temperature of collagen in solid form exceeds 90 °C, it is unlikely for the collagen in ACB to denature in a dry state. Regarding biocompatibility, both ALB and ACB exhibited favorable cytocompatibility, biosafety, and excellent osteogenic repair properties in the results of *in vitro* and *in vivo* studies. In conclusion, given the distinct advantages of ALB and ACB in terms of their respective properties, they have the potential to address the repair needs of load-bearing bone defects in various clinical sites with different clinical requirements.

Biomimetic bone materials play a crucial role in the repair of bone defects. Currently, a wide range of artificial bone materials have been developed and are extensively utilized in clinical practice. However, there is still a clinical need for biomimetic compact bone materials with high strength and toughness. Sufficient structural and mechanical reconstruction is essential for the regeneration of bone defects. Therefore, our research aims to develop biomimetic compact bone materials, which have significant potential in filling bone defects that require mechanical or structural support, such as large cranial defects or segmental bone defects. While dense bone materials provide structural support, they do not offer sufficient space for osteoblasts to migrate towards the interior for regeneration. Achieving a perfect balance between the rate of material degradation and the rate of new bone formation is challenging. The porous structure of bone material is considered essential for bone ingrowth, but it does not meet the mechanical strength requirement. We believe that designing implants with a biphasic composite structure, mimicking the natural combination of cortical and trabecular bone, is an effective approach to address this issue [33]. The porous portion is expected to facilitate rapid ingrowth of new bone and complete bone formation within 3–6 months. The compact portion provides sufficient mechanical support and helps maintain the integrity of the overall structure during the whole process of bone repair. After bone ingrowth, the compact portion becomes enveloped by new bone and is gradually replaced through bone metabolism, resulting in gradual bone remodeling.

Although the ACB exhibits excellent mechanical properties such as high stiffness, hardness, and flexural strength that are comparable to those of natural bone, it still requires improvement in terms of fracture toughness. This insufficiency may be attributed to the absence of the higher level of organization of MC fibrils. While bidirectional freeze-casting can align mineralized collagen microfibrils in parallel, it lacks the higher-scale driving force to assemble mineralized collagen fibrils into fibers, fiber bundles, and plywood-like rotated lamellar structures found in natural bone. Additionally, bone tissue contains numerous trace elements and bioactive compounds, such as magnesium, strontium, silicon, etc., which can enhance bone formation, angiogenesis, and other biological functions [34]. The development of bioactive artificial bone materials is a prominent trend in the field of bone tissue engineering. Currently, our research group is actively working on the development of a bioactive ACB by incorporating MC microfibrils with multiple active elements doped in nHAp. In the future, we plan to combine ACB with either ALB or porous bone material to create biphasic composite bone materials that can be translated into clinical applications for diverse scenarios.

4. Conclusion

In summary, we utilized a cascade of continuous fabrication processes, including biomimetic mineralization of collagen, bidirectional freeze-casting, and pressure-driven fusion, to successfully produce a macroscopic bulk bone material. The MC microfibrils, fabricated through an *in vitro* biomimetic mineralization process, accurately replicate the crystallographic structure of hydroxyapatite and the composition of natural bone at the nanoscale. Subsequently, these microfibrils are aligned in parallel through bidirectional temperature gradients, resulting in a porous and lamellated structure following freeze-drying. Finally, the ACB is formed through high pressure-driven fusion, closely resembling natural cortical bone in terms of composition, hierarchical structure, and mechanical properties. The ACB material exhibits comparable density ($\rho \sim 2.2$ g/cm^3), inorganic content (70.9 wt percent), stiffness ($E_f \sim 25.9$ GPa), hardness ($H \sim 653.1$ MPa), and flexural strength ($\sigma_f \sim 97.8$ MPa) to natural cortical bone. Furthermore, this method is highly feasible, efficient, and more conducive to scalable production. Moreover, the ACB also exhibits excellent mechanical properties in PBS, exceptional biocompatibility, and osteogenic properties *in vivo*, making it well-suited for a broad spectrum of biomedical applications, such as orthopedic, stomatological, and craniofacial surgeries.

Data availability statement

The data that support the findings of this study are available in the supplementary material of this article.

Ethics approval

The animal experiment on rats was approved by the Tsinghua University Institutional Animal Care and Use Committee (IACUC) and followed the Guide for the Care and Use of Laboratory Animals according to the Chinese Ministry of Public Health and U.S. National Institutes of Health Guidelines.

CRediT authorship contribution statement

Lingwenyao Kong: Writing – review & editing, Writing – original draft, Methodology, Investigation. **Yonggang Zhao:** Writing – review & editing, Writing – original draft, Supervision, Software, Methodology, Investigation. **Yang Xiong:** Visualization, Resources, Methodology. **Junlin Chen:** Methodology, Formal analysis. **Shuo Wang:** Software, Methodology. **Ziming Yan:** Visualization, Software, Methodology. **Huibin Shi:** Visualization, Software, Methodology. **Zhanli Liu:** Visualization, Methodology, Investigation. **Xiumei Wang:** Writing – review & editing, Investigation, Funding acquisition.

Declaration of competing interest

The authors declare no conflict of interest.

Acknowledgements

This work was supported by the National Key R&D Program of China (No. 2023YFC2412300 and 2020YFC1107600), the Key R&D Program in Shandong Province (No. 2019JZZY011106), and the Foshan-Tsinghua Industry-University-Research Cooperation Collaborative Innovation Project.

Appendix A. Supplementary data

Supplementary data to this article can be found online at https://doi.org/10.1016/j.bioactmat.2024.02.005.

References

[1] Y. Liu, D. Luo, T. Wang, Small 12 (2016) 4611–4632.
[2] F.Z. Cui, Y. Li, J. Ge, Mat Sci Eng R 57 (2007) 1–27.
[3] X.M. Wang, F.Z. Cui, J. Ge, Y. Wang, J. Struct. Biol. 145 (2004) 236–245.
[4] M.J. Olszta, X. Cheng, S.S. Jee, R. Kumar, Y.Y. Kim, M.J. Kaufman, E.P. Douglas, L. B. Gower, Mat Sci Eng R 58 (2007) 77–116.
[5] J. Peng, Q. Cheng, Adv Mater 29 (2017) 1702959.
[6] J. Peng, Q. Cheng, ChemPhysChem 19 (2018) 1980–1986.
[7] H.D.W.S. Weiner, Annu. Rev. Mater. Sci. 28 (1998) 271–298.
[8] L.B. Mao, H.L. Gao, H.B. Yao, L. Liu, H. Colfen, G. Liu, S.M. Chen, S.K. Li, Y.X. Yan, Y.Y. Liu, S.H. Yu, Science 354 (2016) 107–110.
[9] J. Peng, C. Huang, C. Cao, E. Saiz, Y. Du, S. Dou, A.P. Tomsia, H.D. Wagner, L. Jiang, Q. Cheng, Matter 2 (2020) 220–232.
[10] H. Zhao, S. Liu, Y. Wei, Y. Yue, M. Gao, Y. Li, X. Zeng, X. Deng, N.A. Kotov, L. Guo, L. Jiang, Science 375 (2022) 551–556.
[11] K. Chen, X. Tang, B. Jia, C. Chao, Y. Wei, J. Hou, L. Dong, X. Deng, T.H. Xiao, K. Goda, L. Guo, Nat. Mater. 21 (2022) 1121–1129.
[12] W. Huang, D. Restrepo, J.Y. Jung, F.Y. Su, Z. Liu, R.O. Ritchie, J. McKittrick, P. Zavattieri, D. Kisailus, Adv Mater 31 (2019) e1901561.
[13] S.W. A, W.T. A, H.D.W. B, J. Struct. Biol. 126 (1999) 241–255.
[14] L.-n. Niu, S.E. Jee, K. Jiao, L. Tonggu, M. Li, L. Wang, Y.D. Yang, J.H. Bian, L. Breschi, S.S. Jang, J.H. Chen, David H. Pashley, Franklin R. Tay, Nat. Mater. 16 (2017) 370–378.
[15] P. Simon, D. Gruner, H. Worch, W. Pompe, H. Lichte, T. El Khassawna, C. Heiss, S. Wenisch, R. Kniep, Sci. Rep. 8 (2018) 13696.
[16] Y. Xu, F. Nudelman, E.D. Eren, M.J.M. Wirix, B. Cantaert, W.H. Nijhuis, D. Hermida-Merino, G. Portale, P.H.H. Bomans, C. Ottmann, H. Friedrich, W. Bras, A. Akiva, J.P.R.O. Orgel, F.C. Meldrum, N. Sommerdijk, Nat. Commun. 11 (2020) 5068.
[17] M.E. Launey, P.Y. Chen, J. McKittrick, R.O. Ritchie, Acta Biomater. 6 (2010) 1505–1514.
[18] M.E. Launey, M.J. Buehler, R.O. Ritchie, Annu. Rev. Mater. Res. 40 (2010) 25–53.
[19] Y. Yu, Y. Wang, W. Zhang, H. Wang, J. Li, L. Pan, F. Han, B. Li, Acta Biomater. 113 (2020) 317–327.
[20] C.H. Mac, H.Y. Chan, Y.H. Lin, A.K. Sharma, H.L. Song, Y.S. Chan, K.J. Lin, Y.J. Lin, H.W. Sung, Biomaterials 286 (2022) 121574.
[21] G. Lu, Y. Xu, Q. Liu, M. Chen, H. Sun, P. Wang, X. Li, Y. Wang, X. Li, X. Hui, E. Luo, J. Liu, Q. Jiang, J. Liang, Y. Fan, Y. Sun, X. Zhang, Nat. Commun. 13 (2022) 2499.
[22] Y. Zhao, J. Zheng, Y. Xiong, H. Wang, S. Yang, X. Sun, L. Zhao, A.G. Mikos, X. Wang, Small Struct 4 (2022) 2200256.
[23] Q. Yao, J.G. Cosme, T. Xu, J.M. Miszuk, P.H. Picciani, H. Fong, H. Sun, Biomaterials 115 (2017) 115–127.
[24] Y. Zhao, Y. Xiong, J. Zheng, W. Kongling, J. Chen, C. Li, P. Hu, S. Yang, X. Wang, Biomater. Sci. 11 (2023) 3878–3892.
[25] X. Zhang, B. Wu, S. Sun, P. Wu, Adv. Funct. Mater. 30 (2020) 1910425.
[26] H. Bai, Y. Chen, B. Delattre, A.P. Tomsia, R.O. Ritchie, Sci. Adv. 1 (2015) e1500849.
[27] R.P. Wilkerson, B. Gludovatz, J. Ell, J. Watts, G.E. Hilmas, R.O. Ritchie, Scripta Mater. 158 (2019) 110–115.
[28] R.P. Wilkerson, B. Gludovatz, J. Watts, A.P. Tomsia, G.E. Hilmas, R.O. Ritchie, Acta Mater. 148 (2018) 147–155.
[29] M. Elices, G.V. Guinea, J. Gómez, J. Planas, Eng. Fract. Mech. 69 (2002) 137–163.
[30] K. Park, G.H. Paulino, Appl. Mech. Rev. 64 (2011) 1002.
[31] G. Zi, T. Belytschko (2003), 57, 2221-2240.
[32] R.O. Ritchie, Nat. Mater. 10 (2011) 817–822.
[33] Z. Jingchuan, Z. Zhijun, Y. Yongdong, W. Shuo, Z. Yonggang, X. Yang, Y. Shuhui, Q. Zhiye, S. Tianxi, Z. Chunyang, Regen Biomater 9 (2022) rbac004.
[34] X. Shen, Y. Zhang, Y. Gu, Y. Xu, Y. Liu, B. Li, L. Chen, Biomaterials 106 (2016) 205–216.